Ceramics

Exploring the links between crystal chemistry, cesium retention, thermochemistry and chemical durability in single-phase (Ba,Cs)$_{1.33}$(Fe,Ti)$_8$O$_{16}$ hollandite

Mingyang Zhao[1], Patrick Russell[1], Jake Amoroso[2], Scott Misture[3], Stephen Utlak[4,6], Theodore Besmann[4], Lindsay Shuller-Nickles[5], and Kyle S. Brinkman[1,*]

[1] Department of Materials Science and Engineering, Clemson University, Clemson, SC 29634, USA

[2] Savannah River National Laboratory, Aiken, SC 29808, USA

[3] Kazuo Inamori School of Engineering, Alfred University, Alfred, NY 14802, USA

[4] Nuclear Engineering Program, Department of Mechanical Engineering, University of South Carolina, Columbia, SC 29208, USA

[5] Department of Environmental Engineering and Earth Sciences, Clemson University, Clemson, SC 29634, USA

[6] Present address: Materials Science and Technology Division, Oak Ridge National Laboratory, Oak Ridge, TN 37931, USA

ABSTRACT

A series of single-phase Fe-substituted hollandite (Ba,Cs)$_{1.33}$(Fe,Ti)$_8$O$_{16}$ compositions with the chemical formula Ba$_{1.33-x}$Cs$_x$Fe$_{2.66-x}$Ti$_{5.34+x}$O$_{16}$ (x = 0, 0.1, 0.2, 0.667, and 1.33) were systematically investigated using both experimental and computational methods to establish possible links between crystal chemistry, Cs retention, thermochemistry and chemical durability. A phase transition from monoclinic to tetragonal was observed as a function of both Cs content and temperature. Elemental analysis revealed that Cs retention was significantly improved for the hollandite with higher Cs content. High-temperature melt solution calorimetry and sublattice-based thermodynamic simulations confirmed a high degree of thermodynamic stability in the Fe-substituted compounds which was enhanced in compositions with higher Cs content. This trend can be primarily attributed to two factors: (1) a decreasing ratio of the average ionic radii of B-site cations to that of A-site cations and (2) an increasing tolerance factor. Based on a reoptimized sublattice model, a pseudo-ternary phase diagram was generated to predict the optimal composition possessing the highest Cs content and A-site occupancy, which had not been experimentally explored. Leaching tests further verified that high Cs-containing compositions have significant chemical durability.

Address correspondence to E-mail: ksbrink@clemson.edu

🖄 Springer

Introduction

Hollandite is a promising family of crystalline ceramic materials used to immobilize radioactive alkali and alkaline earth elements (e.g., Cs and Ba) in high-level waste (HLW). Compared to borosilicate glasses currently used as commercial waste matrices, hollandite-based ceramics present superior thermodynamic stability and chemical durability, and higher Cs loading [1–7].

Hollandite has the general formula $A_x^{+/2+}(B^{2+/3+/4+}, Ti^{4+})_8 O_{16}$, where $0 \leq x \leq 2$. A-sites are occupied by Cs^+ and (or) Ba^{2+}, and numerous cations with different valences can be substituted for Ti^{4+} on B-sites, such as Zn^{2+}, Al^{3+}, Fe^{3+}, Ga^{3+} and Cr^{3+} [4, 5, 8–11]. The hollandite structure consists of eight corner and edge sharing $(B,Ti)O_6$ octahedra, which interlink and form a three-dimensional framework with 2×2 tunnels to accommodate A-site cations [4, 9, 10, 12]. Hollandite can adopt either a tetragonal (space group $I4/m$) or a monoclinic (space group $I2/m$) symmetry depending on the ratio of the average ionic radii of B-site cations to that of A-site cations (R_B/R_A). When tunnel cations are large enough, the framework exhibits shear-type collapse and the tetragonal symmetry will reduce to a monoclinic symmetry [2].

Although a wide range of hollandites have been fabricated, many potential issues still exist [13] including the appearance of secondary and Cs-parasitic phases [9, 14], severe Cs loss [9] and the requirement for elevated temperatures during melt-processing [14]. An Fe-substituted hollandite is a promising candidate according to several studies [2, 8, 9, 15] over the past decade. Firstly, the melting point of Fe_2O_3 (~ 1565 °C) is much lower than that of refractory oxides (e.g., Al_2O_3, MgO, Cr_2O_3, etc.) used to form other types of hollandite. Therefore, it should be easier to obtain dense Fe-substituted hollandite via conventional sintering as well as reduce the temperature for melt-processing. Secondly, the ionic radius difference between Fe^{3+} and Ti^{4+} on B-sites provides a large enough space for Cs^+ cations to be accommodated into the tunnel structure without forming Cs-parasitic phases as compared to Al- and Ga-substituted hollandites [8, 9, 15].

Thermodynamic stability and chemical durability are two vital properties for assessing the performance of waste forms. Several related studies have been conducted on Al-, Zn- and Ga-substituted hollandites

[2–5, 16, 17]; however, there is little information on Fe-substituted hollandite [2]. In this work, a broad compositional range of single-phase Fe-substituted hollandite $(Ba,Cs)_{1.33}(Fe,Ti)_8 O_{16}$ phases from the Ba end member to the Cs end member was successfully synthesized via solid-state reactions. Changes in the crystal chemistry as a function of Cs content and temperature were analyzed by high-temperature X-ray diffraction and high-temperature Raman spectroscopy. Cs retention was determined by energy dispersive X-ray spectroscopy measurements. Enthalpies of formation from constituent oxides were measured by high-temperature oxide melt solution calorimetry. Results from calorimetric measurements were reinforced by calculations based on a reoptimized sublattice model. An isothermal pseudo-ternary diagram was subsequently generated from the reoptimized sublattice model as an example to demonstrate its capability to extrapolate phase equilibrium behavior to regions not yet experimentally explored. Effects of ratio of the average ionic radii of B-site cations to that of A-site cations (R_B/R_A), tolerance factor (t_H), optical basicity (Λ) and symmetry on enthalpies of formation were discussed. Furthermore, phase formation and stability of Fe-substituted hollandite with respect to other competing phase assemblages were estimated. Finally, chemical durability was measured by a leaching test.

Experimental

Sample synthesis

A series of Fe-substituted hollandite with the chemical formula $Ba_{1.33-x}Cs_x Fe_{2.66-x} Ti_{5.34+x} O_{16}$ ($x = 0$, 0.1, 0.2, 0.667, and 1.33) were synthesized using a solid-state reaction route (as shown in Table 1). For

Table 1 Target and analyzed EDS compositions of hollandite samples

Sample	Target composition	EDS composition
H1	$Ba_{1.33}Fe_{2.66}Ti_{5.34}O_{16}$	$Ba_{1.35}Fe_{2.65}Ti_{5.33}O_{16}$
H2	$Ba_{1.23}Cs_{0.1}Fe_{2.56}Ti_{5.44}O_{16}$	$Ba_{1.23}Cs_{0.07}Fe_{2.57}Ti_{5.44}O_{16}$
H3	$Ba_{1.13}Cs_{0.2}Fe_{2.46}Ti_{5.54}O_{16}$	$Ba_{1.12}Cs_{0.16}Fe_{2.48}Ti_{5.54}O_{16}$
H4	$Ba_{0.667}Cs_{0.667}Fe_2 Ti_6 O_{16}$	$Ba_{0.69}Cs_{0.59}Fe_{2.01}Ti_6 O_{16}$
H5	$Cs_{1.33}Fe_{1.33}Ti_{6.67}O_{16}$	$Cs_{1.27}Fe_{1.35}Ti_{6.67}O_{16}$

Compositions were normalized to Ti and oxygen contents were corrected to achieve charge balance

simplicity, they are denoted as $Ba_{1.33}Fe_{2.66}Ti_{5.34}O_{16}$ (H1), $Ba_{1.23}Cs_{0.1}Fe_{2.56}Ti_{5.44}O_{16}$ (H2), $Ba_{1.13}Cs_{0.2}Fe_{2.46}$-$Ti_{5.54}O_{16}$ (H3), $Ba_{0.667}Cs_{0.667}Fe_2Ti_6O_{16}$ (H4), and $Cs_{1.33}Fe_{1.33}Ti_{6.67}O_{16}$ (H5) throughout this paper.

Reagent-grade powders of barium carbonate, $BaCO_3$ (Sigma-Aldrich, 99.98%), cesium carbonate, Cs_2CO_3 (Alfa Aesar, 99.9%), iron(III) oxide, Fe_2O_3 (Alfa Aesar, 99.9%) and titanium oxide (anatase), TiO_2 (Inframat Advanced Materials, 99.9%) were used as starting materials. Stoichiometric amounts of raw powders were mixed and added into high-density polyethylene (HDPE) bottles with ethyl alcohol and yttrium-stabilized zirconia (YSZ) grinding media (Inframat Advanced Materials) for 24 h. The post-ball milling slurry was dried in an oven overnight. As-dried powders were ground in an agate mortar and pestle. Heat treatment processes, including calcination and sintering, were performed in a box furnace. Hollandite samples were prepared as follows: (1) H1–H5 were calcined in air at 1000 °C for 5 h to decompose carbonates, then wet ball milled for another 24 h and dried again, (2) the dried H1 was ground, cold pressed into pellets, and sintered in air at 1300 °C for 5 h; (3) the dried H2–H5 were ground, cold pressed into pellets, and sintered in air at 1200 °C for 5 h. To reduce potential volatilization of Cs and Ba at elevated temperatures during sintering, alumina crucibles were covered with alumina lids and the pressed pellets were immersed in additional calcined powders. As-sintered pellets H1–H5 were crushed and ground into powders for further experiments.

To study whether sintering impacted enthalpies of formation, selected samples were directly synthesized in a box furnace as powder samples. Specifically, remaining powder sample H1 obtained after step (1) was calcined at 1300 °C for 5 h, while remaining powder samples H4 and H5 obtained after step (1) were calcined at 1200 °C for 5 h. These calcined powder samples H1, H4, and H5 were denoted as H1 (C), H4 (C), and H5 (C), respectively, and only used for calorimetric measurements described in "Calorimetric measurements" section.

Characterization

Room temperature X-ray diffraction (RT-XRD) measurements were conducted by Rigaku Ultima IV diffractometer with monochromatic Cu Kα radiation ($\lambda = 1.54$ Å) to analyze the crystal structure of hollandite samples H1–H5. The data were collected from 15° to 70° 2θ with a 0.02° step size. Microstructure and chemical composition of hollandite samples were investigated by a Hitachi SU6600 scanning electron microscopy (SEM) equipped with energy dispersive X-ray spectroscopy (EDS) analysis (Oxford). Samples were not coated prior to EDS measurements to avoid contamination. EDS composition was reported as the average composition of at least ten different sites over representative X-ray microstructure maps. Back-scattered electron (BSE) imaging mode was selected to observe homogeneity and morphology of samples. Inductively coupled plasma-mass spectroscopy (ICP-MS) was used to measure Cs concentrations in leaching solution, and inductively coupled plasma-atomic emission spectroscopy (ICP-AES) was used to measure Ba, Ga, and Ti concentrations in leaching solution. A lithium metaborate (LM) fusion preparation with nitric acid digestion was used to dissolve solid samples for ICP-MS and ICP-AES analysis for leaching tests.

To study evolution of the bulk structure as a function of temperature, high temperature (HT)-XRD was performed on H1–H4 using monochromatic Cu Kα radiation in a Bruker D8 Advance diffractometer with an Anton Paar HTK 1200 heating stage. Powder samples were mounted on a high purity (99.6%) alumina sample plate. Data were collected using a fixed divergence slit in the range of $10° \leq 2\theta \leq 80°$ with a 0.025° step size. The measured samples were first heated from RT to 450 °C with an increment of 25 °C and then to 1000 °C with an increment of 50 °C, afterward the samples were cooled to 400 °C with an increment of 100 °C, to 250 °C with an increment of 50 °C, and then to RT with an increment of 25 °C.

Evolution of local structure with different temperatures was also recorded by HT-Raman spectroscopy with 20-second integration time and 20 accumulations using a WITec instrument with 633 nm laser and 5 mw output power. H1 and H2 were heated up from RT to 350 and 150 °C, respectively, which were high enough to induce the $M–T$ phase transition. The Linkam scientific instruments were used as temperature assembly with link 1.2.5.1300 software used for temperature control with accuracy ± 1 °C. Enthalpy (ΔH_c) of the monoclinic–tetragonal ($M–T$) phase transition of samples H1 and H2 was determined by Netzsch 404 C Pegasus DSC to assess their effect on thermodynamic stability. Samples were placed in alumina crucibles, heated to 500 °C at first, then cooled down to 100 °C and held for 10 min under dry

Ar atmosphere to exclude the potential heat effect from water content. Afterward, the samples were heated up to 500 °C and cooled down to RT again. The baseline of the same empty alumina crucible under the same experimental condition was recorded for subtraction.

High-temperature oxide melt solution calorimetry

High-temperature oxide melt solution calorimetry was performed using an AlexSYS 1000 calorimeter (SETARAM) operating at 702 °C. In a drop solution calorimetry experiment, approximately 5 mg weighed powder sample was loosely pressed into pellets and dropped from room temperature into the molten sodium molybdate ($3Na_2O \cdot 4MoO_3$) solvent in a platinum crucible in the calorimeter. Detailed instrument and experimental procedure can be found by Navrotsky [18, 19]. To stir the melt and improve sample dissolution, the calorimeter assembly was flushed with dry air at ∼ 48 mL/min and dry air was bubbled through the solvent at ∼ 5 mL/min. At least six successful drops were performed for each composition to obtain statistically reliable data. The calorimeter was calibrated utilizing the heat content of high purity α-aluminum oxide (Alfa Aesar, 99.997%). This methodology is well established and has been described in prior reports [18, 19].

Leaching test

Leaching tests following guidelines of the product consistency test (PCT) (Method-B) were performed on H1 and H3–H5 to assess aqueous chemical durability [20, 21]. Samples were ground and washed with water. As-prepared samples with a constant 1:10 ratio of sample mass to water volume were placed in stainless steel vessels. The vessels were closed, sealed, and placed in an oven at 90 ± 2 °C for 7 days. Once cooled, post-leaching solutions were analyzed. For each composition, three replicates were prepared to acquire reliable data. Normalized elemental release (NL) was calculated using Eq. (1):
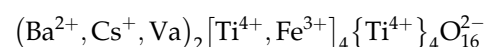
$$NL_i = \frac{C_i \times V}{f_i \times SA} \tag{1}$$

where NL_i = normalized elemental release (g/m^2) of element "i" (e.g., Cs and Ba), C_i = concentration of element "i" in post-leached solution (g/L),

f_i = measured fraction of element "i" in pre-leached samples (unitless), SA = surface area of samples (m^2), and V = water volume (mL). Specific surface area of each crushed sample was measured by Brunauer–Emmett–Teller (BET) analysis. It is notable that fractional elemental release (FR) values for Ga-substituted hollandite instead of NL values were reported in our previous publication [4]. In prior work, the FR values were more accurate than NL values, because the surface areas were estimated based on particle sizes after sieving. In this work, however, specific surface areas were accurately measured via the BET method and thereby NL values were reported.

Development and reoptimization of sublattice model

A set of thermodynamic functions were generated by Utlak et al. [22] based on the calculation of phase diagrams (CALPHAD) methodology which successfully characterized the equilibrium behavior of hollandite compositions considered for potential HLW systems. Within that effort, a sublattice model was further developed using the compound energy formalism (CEF) to represent the non-stoichiometry of the hollandite solid solution phase, which was based on the hollandite general formula $A_2B_8O_{16}$ where A is a monovalent or divalent atom, and B has a valence between 2 and 5 [9, 14]. In the current effort, the model is constrained such that only Fe^{3+} and Ti^{4+} are present on the B-sites of the Fe-substituted hollandite [11]. Hence, a four sublattice CEF hollandite model can be defined as:

$$\left(Ba^{2+}, Cs^+, Va\right)_2 \left[Ti^{4+}, Fe^{3+}\right]_4 \left\{Ti^{4+}\right\}_4 O_{16}^{2-}$$

where Va represents tunnel vacancies. Details regarding the hollandite CEF sublattice model and potential to obtain Gibbs energies for hollandite compositions have been described by Utlak et al. [22].

Although enthalpies of formation of Fe-substituted hollandites were previously reported by Utlak et al. [22] based on the sublattice model, it was necessary to reoptimize the original model considering the experimentally determined data of the current effort to derive reliable calculated values. Consequently, the Gibbs energies of hollandite end members as well as Ba and Cs titanate end members also needed to be correspondingly adjusted to well represent enthalpies of formation (Table S1) while retaining good agreement between the computed and measured Fe-

hollandite stoichiometries obtained by Utlak et al. [22].

Results and discussion

Crystallography

Room temperature XRD patterns of synthesized samples H1–H5 described in Table 1 are displayed in Fig. 1a. The spectra indicate single-phase hollandite with either a tetragonal (space group: $I4/m$) or monoclinic (space group: $I2/m$) structure, depending on the level of Cs substitution for Ba (as shown in Table 2). BaFeTi$_7$O$_{16}$ (PDF#53-1179) and Ba$_4$Fe$_8$Ti$_{16}$O$_{48}$ (PDF#51-1899) were used as model structures of tetragonal and monoclinic, respectively. In Fig. 1a, two major families of lattice planes {310} and {220} of samples H1–H5 displayed a shift to smaller 2θ. This shift indicates that the unit cell expands with increasing Cs content, which has been confirmed by

prior studies [4, 5, 10, 11, 23, 24]. Moreover, H1 and H2 are monoclinic, while H3–H5 are tetragonal. The inset in Fig. 1a clearly shows that intensity of monoclinic planes—(−202), (202), (−301), (301), (−103), and (103)—is gradually reduced and then they are merged into tetragonal planes—(220) and (310)—which indicates that the $M–T$ phase transition occurs as the Cs content increases.

It is attractive to establish a general guideline which can effectively demarcate tetragonal and monoclinic regions, since monoclinic hollandite is reported to be less stable than the tetragonal analogues according to previous studies [2, 5, 25]. Two prior models have been used to predict the symmetries of hollandite since the 1980s, Post et al. [26] and Zhang and Burnham [27], respectively. However, Zhang and Burnham's tetragonal criterion is generally considered more applicable due to a number of exceptions that have been found in the model of Post et al. [27]. According to this criterion, hollandite
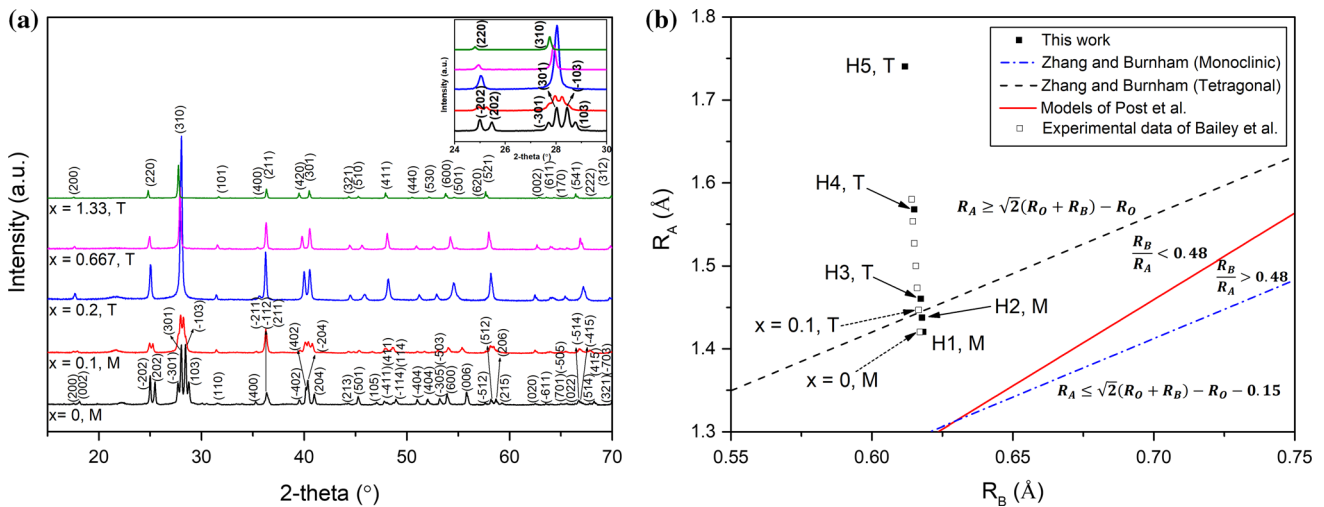

Figure 1 **a** RT-XRD patterns of H1–H5 with different Cs content; **b** According to Zhang and Burnham's prediction [28], the region above the black dash corresponds to tetragonal and the region below the blue dot dash line corresponds to monoclinic, while the region between the lines is an undetermined zone. The red straight line is the criterion predicted by Post et al. [27]. The data labeled as black squares are from this work, and the data displayed as open square are from Bailey et al. [12] T and M are short for tetragonal and monoclinic, respectively.

Table 2 Crystal structure, average ionic radius of cations on A-sites (R_A) and B-sites (R_B), the ratio of R_B/R_A, t_H, and Λ_H of samples H1–H5

Sample	Crystal structure	R_A (Å)	R_B (Å)	R_B/R_A	t_H	Λ_H
H1	Monoclinic	1.420	0.618	0.435	0.984	0.788
H2	Monoclinic	1.437	0.618	0.430	0.992	0.789
H3	Tetragonal	1.460	0.617	0.423	1.003	0.789
H4	Tetragonal	1.568	0.615	0.392	1.055	0.790
H5	Tetragonal	1.740	0.612	0.352	1.136	0.792

adopts tetragonal if $R_A > \sqrt{2}(R_O + R_B) - R_O$ [27]. To better illustrate the phase boundary of the M–T transition in this work, Fig. 1b was drawn where R_B and R_A were calculated using the Shannon effective ionic radii: $Ba^{2+} = 1.42$ Å and $Cs^+ = 1.74$ Å in eightfold coordination, while $Fe^{3+} = 0.645$ Å (high spin) and $Ti^{4+} = 0.605$ Å in sixfold coordination (Table 2) [15]. In Fig. 1b, H3–H5 having tetragonal symmetry fall into the tetragonal region as expected, while H1 and H2 exhibiting monoclinic symmetry are located in the undetermined region where hollandite could adopt either monoclinic or tetragonal symmetry. Moreover, a similar investigation of Cs content-dependent M–T phase transition of $Ba_{1.2-x}Cs_xFe_{2.4-x}Ti_{5.6+x}O_{16}$ ($0 \leq x \leq 0.6$) hollandite was reported by Bailey et al. [11]. Due to the uncertain symmetry in the mixed phase region, Zhang and Burnham's tetragonal criterion is an effective guideline to follow when intentionally designing tetragonal hollandite-based waste forms.

HT-XRD spectra of H1–H4 with partial 2θ range are shown in Fig. 2a–d to clearly show the evolution of the symmetry change at different temperatures. Monoclinic peaks of H1 and H2 within the 2θ range of 24°–30° transform into the tetragonal peak when temperature was within 300–350 °C and 75–150 °C, respectively, which indicates that an apparent M–T phase transition occurred for both H1 and H2. Moreover, this M–T phase transition is fully reversible because the symmetry recovers from tetragonal to monoclinic when the temperature cooled down to RT. For H3 and H4, their tetragonal symmetries remained during the entire heating and cooling steps. The HT-XRD spectra of H1–H4 with full 2θ range are displayed in Figure S1.

HT-Raman spectra of the sample H1 and H2 are displayed in Fig. 3a, b, and frequencies and mode assignments of their main Raman bands are listed in Table S2. For the RT-Raman spectrum of H1 in Fig. 3a, five major bands were observed at ~ 83, ~ 130, ~ 367, ~ 556 and ~ 700 cm^{-1}, while a small
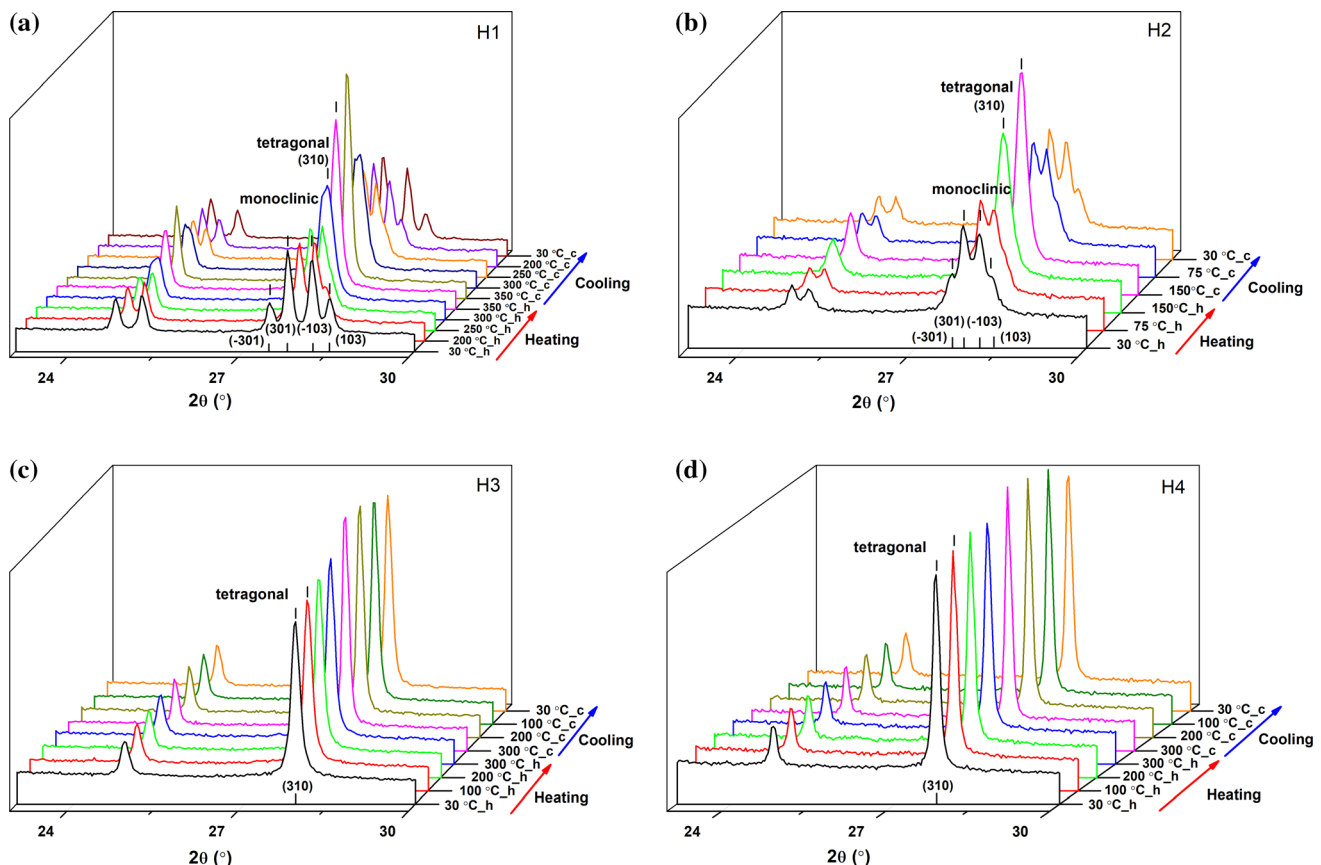

Figure 2 HT-XRD spectra with partial 2θ range of **a** H1, **b** H2, **c** H3 and **d** H4 displaying evolution of long-range structural change during heating and cooling steps.
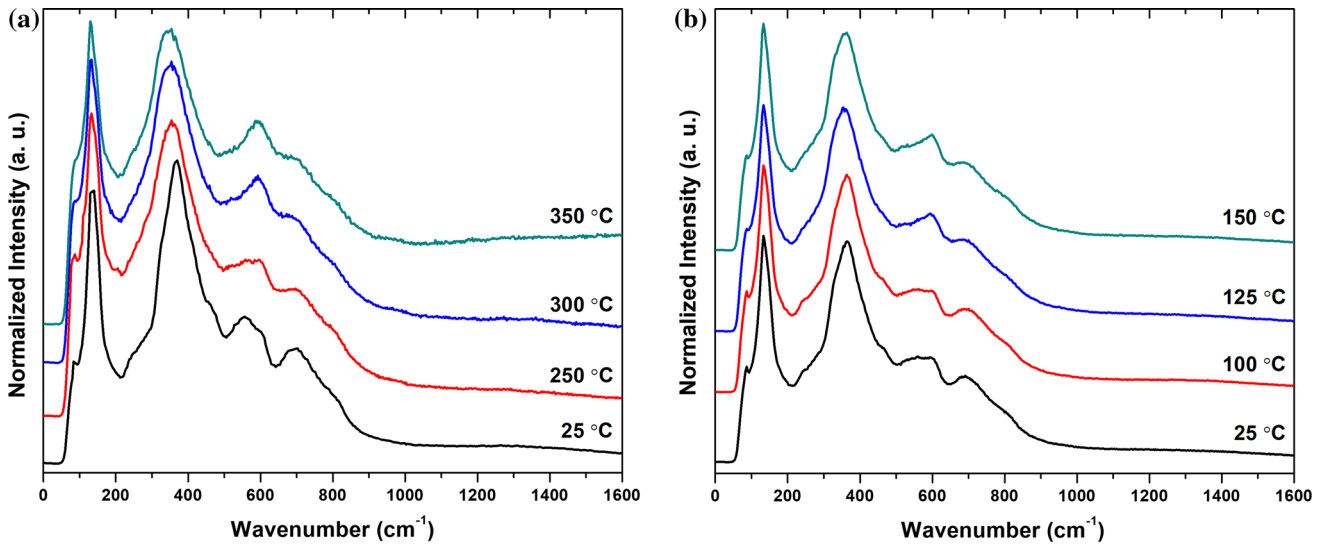
Figure 3 HT-Raman spectra of **a** H1 and **b** H2 over the temperature range where the *M–T* phase transition occurs.

shoulder appeared at ~ 600 cm^{-1}. The band at ~ 83 cm^{-1} is assigned as the vibration mode of tunnel cations (i.e., Ba) [28]. The peak at ~ 130 cm^{-1} may be attributed to (Fe,Ti)-O symmetric stretching of (Fe,Ti)O$_6$ octahedra, while three peaks at ~ 367, ~ 556 and ~ 700 cm^{-1} and the shoulder peak ~ 600 cm^{-1} might arise from the bending mode of (Fe,Ti)O$_6$ octahedra [28–34]. A number of changes in the Raman spectra across the *M–T* phase were observed. The intensity of the band ~ 83 cm^{-1} at RT increased and it shifted to higher wavenumber with increasing temperature, indicating that the interaction between Ba and (Fe,Ti)O$_6$ octahedra framework becomes stronger [28]. Moreover, the bandwidth of the band at ~ 130 cm^{-1} at RT became slightly broader, implying changes in the symmetric stretching modes due to the (Fe,Ti)O$_6$ octahedra and the *M–T* phase transition as temperature increased [34]. The bending mode of (Fe,Ti)O$_6$ octahedra was also affected by the *M–T* phase transition as follows: (1) the band at ~ 367 cm^{-1} (RT) shifts to lower wavenumber, (2) the intensity of the band ~ 556 cm^{-1} (RT) gradually decreases, and (iii) the intensity of the shoulder peak ~ 600 cm^{-1} (RT) gradually increases. In addition, the band appearing at relatively high wavenumber ~ 700 cm^{-1} becomes less intense as the temperature increases, due to the monoclinic to tetragonal phase transition [34]. Similar changes of Raman bands at different temperatures of H2 are also reflected in Fig. 3b. Consequently, features of the *M–T* phase transition could be observed

both in the long-range ordering as well as the short-range ordering.

Elemental analysis and Cs retention

The elemental concentrations of Ba, Cs, Fe, and Ti of hollandite samples were measured by EDS as shown in Table 1. Some representative sites on the EDS microstructure map of H4 in Figure S2 were selected to serve as an example to illustrate the method. In addition, X-ray elemental maps of H4 in Figure S3 were selected as representatives to evaluate the homogeneity of the elemental distribution. The results generally confirm that nominal stoichiometries were achieved and the elemental distribution in samples was homogeneous. The actual compositions listed in Table 1 were used to calculate enthalpies of formation of H1–H5 in "Calorimetric measurements" section. Figure S4 displays BSE images of H1–H5 revealing no occurrence of distinct phase segregation or secondary phases.

Cs loss is one of the most critical issues when hollandite pellets are sintered at elevated temperatures. Therefore, Cs retention of the post-sintering pellets H2–H5 (H1 did not have Cs content) was determined by EDS measurements and is presented in Fig. 4. It was found that Cs retention was significantly improved in compositions with higher Cs content indicating that Cs could be more favorably incorporated into the hollandite structure rather than through volatilization which agrees with our previous study of Zn-substituted hollandite [5]. Higher Cs
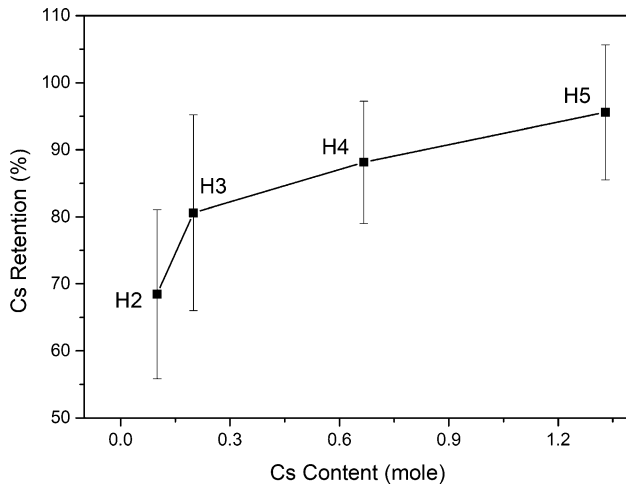
Figure 4 Cs retention in the post-sintering samples H2–H5 as determined by EDS measurements (experimental errors were estimated by two standard deviations of the average of the actual Cs content).

Table 4 Enthalpies of drop solution in $3Na_2O \cdot 4MoO_3$ solvent at 702 °C (ΔH_{ds}) and enthalpies of formation from the elements ($\Delta H_{f,el}$) at 25 °C of related binary constituent oxides

Oxide	ΔH_{ds} (kJ/mol)	$\Delta H_{f,el}$ (kJ/mol)
BaO	-184.61 ± 3.21	-548.1 ± 2.1
Cs_2O	-348.9 ± 1.7	-346.0 ± 1.2
α-Fe_2O_3	95.63 ± 0.50	-826.2 ± 1.3
TiO_2	60.81 ± 0.11	-944.0 ± 0.8

retention appears to be linked to enhanced thermodynamic stability of the hollandite phase with higher Cs content, which has been confirmed by calorimetric measurements presented in "Calorimetric measurements" section.

Thermochemistry

Calorimetric measurements

The enthalpies of drop solution (ΔH_{ds}) of H1–H5 measured in the molten $3Na_2O \cdot 4MoO_3$ solvent at 702 °C were given in Table 3. Using these values and previously reported ΔH_{ds} values and the enthalpies of formation at 25 °C from the elements ($\Delta H_{f,el}$) data for BaO, Cs_2O, α-Fe_2O_3 and TiO_2 (shown in Table 4), the enthalpies of formation at 25 °C from the constituent oxides ($\Delta H_{f,ox}$) and $\Delta H_{f,el}$ values of hollandite were calculated using thermochemical cycles (e.g., those for H4 with actual EDS compositions as shown

in Table 5) [35–39]. In Fig. 5a, $\Delta H_{f,ox}$ values of H1–H5 are all strongly exothermic, indicating that they are thermodynamically stable relative to the constituent oxides. Moreover, $\Delta H_{f,ox}$ values become increasingly exothermic with increasing Cs substitution. It is worth noting that significantly negative enthalpy is the dominating term in the Gibbs free energy in solid-state reaction synthesis, because the overall contribution from changes of the entropic term (including both vibrational and configurational entropic changes) is very small at temperatures below 700 °C [2]. Therefore, it is convincing that the hollandite with higher Cs content is more energetically stable [2, 40].

Calorimetric measurements were also performed for the calcined powder samples H1 (C), H4 (C), and H5 (C) in order to investigate whether the enthalpy of formation of hollandite was affected by different processing conditions (i.e., calcination versus sintering). Actual compositions of the three calcined samples were also measured by EDS and are given in Table S3. $\Delta H_{f,ox}$ values of the three calcined samples were calculated by the same approach used for the sintered samples and are displayed in Table S4. Figure 5b clearly shows a consistent trend for both sintered and calcined samples, which is that the hollandite with higher Cs substitution has more negative enthalpy of formation and thereby enhanced

Table 3 Enthalpies of drop solution (ΔH_{ds}) in $3Na_2O \cdot 4MoO_3$ solvent at 702 °C and enthalpies of formation from constituent oxides ($\Delta H_{f,ox}$) and from the elements ($\Delta H_{f,el}$) of five hollandite compositions at 25 °C

Sample	ΔH_{ds} (kJ/mol)	$\Delta H_{f,ox}$ (kJ/mol)	$\Delta H_{f,el}$ (kJ/mol)	ΔH_{rxn} (kJ/mol)
H1	398.60 ± 3.87 (8)	-196.67 ± 5.88	-7067.03 ± 7.99	-8.93 ± 8.89
H2	403.09 ± 5.20 (8)	-188.68 ± 6.62	-7071.98 ± 8.49	1.35 ± 9.07
H3	416.00 ± 8.33 (6)	-195.21 ± 9.14	-7091.01 ± 10.55	24.63 ± 10.99
H4	442.05 ± 9.26 (6)	-211.39 ± 9.57	-7185.98 ± 10.89	106.30 ± 7.72
H5	482.43 ± 7.91 (6)	-234.03 ± 8.03	-7304.79 ± 9.71	N/A[a]

Uncertainty is two standard deviations of the mean and the value in parentheses is the number of experiments

[a] ΔH_{rxn} of the H5 was non-available (N/A) due to the lack of Ba cations on A-sites

Table 5 Thermochemical cycles used for calculation of enthalpies of formation of the sample H4 from constituent oxides ($\Delta H_{f,ox}$) and from the elements ($\Delta H_{f,el}$) at 25 °C with correction based on EDS analyzed composition in Table 1

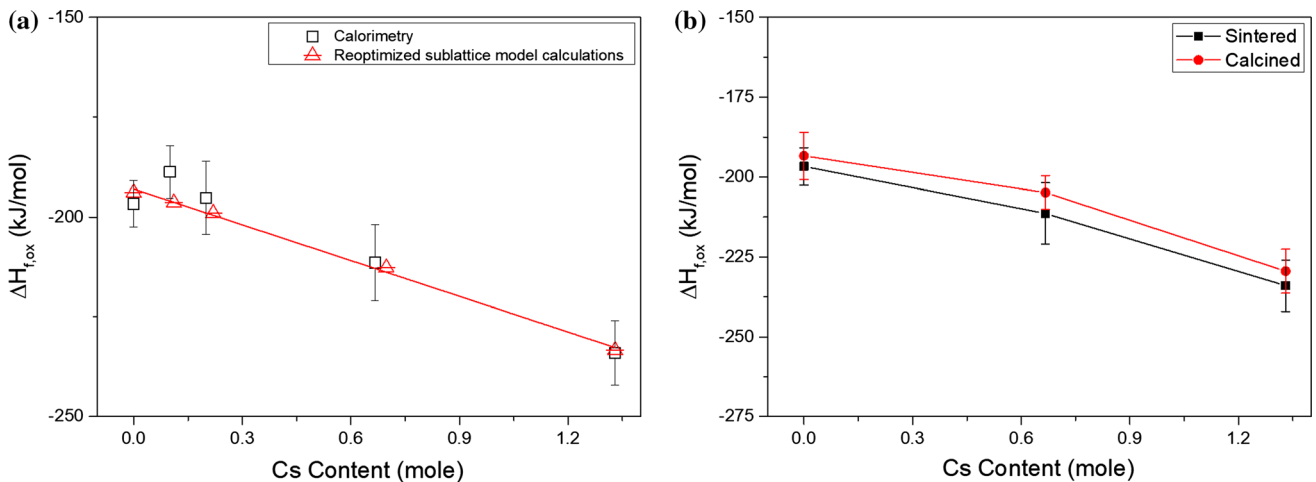|	
Enthalpy of formation of the sample H4 from its constituent oxides at 25 °C ($\Delta H_{f,ox}$)	
$Ba_{0.69}Cs_{0.59}Fe_{2.01}Ti_6O_{16}$ (s,25 °C) → 0.69 BaO (sln,702 °C) + 0.295 Cs_2O (sln,702 °C) + 1.005 Fe_2O_3 (sln,702 °C) + 6 TiO_2 (sln,702 °C)	ΔH_{ds}
0.69 BaO (s,25 °C) → 0.69 BaO (sln,702 °C)	ΔH_1
0.295 Cs_2O (s,25 °C) → 0.295 Cs_2O (sln,702 °C)	ΔH_2
1.005 Fe_2O_3 (s,25 °C) → 1.005 Fe_2O_3 (sln,702 °C)	ΔH_3
6 TiO_2 (s,25 °C) → 6 TiO_2 (sln,702 °C)	ΔH_4
0.69 BaO (s,25 °C) + 0.295 Cs_2O (s,25 °C) + 1.005 Fe_2O_3 (s,25 °C) + 6 TiO_2 (s,25 °C) → $Ba_{0.69}Cs_{0.59}Fe_{2.01}Ti_6O_{16}$ (s,25 °C)	$\Delta H_{f,ox}$
$\Delta H_{f,ox} = \sum \Delta H_i$ $(i = 1–4) - \Delta H_{ds}$	
Enthalpy of formation of H4 from the elements at 25 °C ($\Delta H_{f,el}$)	
0.69 BaO (s,25 °C) + 0.295 Cs_2O (s,25 °C) + 1.005 Fe_2O_3 (s,25 °C) + 6 TiO_2 (s,25 °C) → $Ba_{0.69}Cs_{0.59}Fe_{2.01}Ti_6O_{16}$ (s,25 °C)	$\Delta H_{f,ox}$
0.69 Ba (s,25 °C) + 0.345 O_2 (g,25 °C) → 0.69 BaO (s,702 °C)	ΔH_5
0.59 Cs (s,25 °C) + 0.1475 O_2 (g,25 °C) → 0.295 Cs_2O (s,702 °C)	ΔH_6
2.01 Fe (s,25 °C) + 1.5075 O_2 (g,25 °C) → 1.005 Fe_2O_3 (s,702 °C)	ΔH_7
6 Ti (s,25 °C) + 6 O_2 (g,25 °C) → 6 TiO_2 (s,702 °C)	ΔH_8
0.69 Ba (s,25 °C) + 0.59 Cs (s,25 °C) + 2.01 Fe (s,25 °C) + 6 Ti (s,25 °C) + 8 O_2 (g,25 °C) → $Ba_{0.69}Cs_{0.59}Fe_{2.01}Ti_6O_{16}$ (s,25 °C)	$\Delta H_{f,el}$
$\Delta H_{f,el} = \Delta H_{f,ox} + \sum \Delta H_i$ $(i = 5–8)$	

Figure 5 **a** The trends for values of experimental enthalpies of formation from the constituent oxides at 25 °C ($\Delta H_{f,ox}$) for H1–H5; **b** the comparison of enthalpies of formation for selected sintered and calcined samples.

thermodynamic stability. It is notable that the $\Delta H_{f,ox}$ difference between the calcined and sintered samples is small enough to be neglected compared with experimental errors.

Calculated enthalpies of formation based on sublattice model

$\Delta H_{f,el}$ values of H1–H5 calculated using the sublattice model are listed in Table 6. $\Delta H_{f,ox}$ values of H1–H5 were derived by subtracting the sum of the oxide formation enthalpies from the elements shown in

Table 4 from the $\Delta H_{f,el}$ values in Table 6. In a similar manner as the approach illustrated in Table 5, each oxide formation enthalpy was multiplied by a coefficient to obtain the calculated hollandite stoichiometries reported in Table 6 prior to being summed. As indicated by Fig. 5a, $\Delta H_{f,ox}$ values derived from this thermodynamic model represent the same fundamental trends observed in the experimental results.

It is notable that reoptimization of the sublattice model did not alter computed compositional results for non-melt processed Fe-substituted hollandite

Table 6 Standard enthalpies of formation from constituent oxides ($\Delta H_{f,ox}$) and from the elements ($\Delta H_{f,el}$) for Fe-substituted hollandite calculated from the thermodynamic database

Sample	Calculated composition	$\Delta H_{f,ox}$ (kJ/mol)	$\Delta H_{f,el}$ (kJ/mol)
H1	$Ba_{1.16}Fe_{2.32}Ti_{5.68}O_{16}$	-193.91	-7149.55
H2	$Ba_{1.07}Cs_{0.111}Fe_{2.25}Ti_{5.75}O_{16}$	-196.39	-7159.72
H3	$Ba_{0.978}Cs_{0.220}Fe_{2.18}Ti_{5.82}O_{16}$	-198.99	-7170.06
H4	$Ba_{0.573}Cs_{0.698}Fe_{1.84}Ti_{6.16}O_{16}$	-212.70	-7220.35
H5	$Cs_{1.33}Fe_{1.33}Ti_{6.67}O_{16}$	-233.35	-7309.34

reported by Utlak et al. [22]. Unlike the prior melt-processed hollandite, the Cs-parasitic phase $CsAlTiO_4$ was not observed in this work. Nevertheless, the refined model indeed slightly impacts the computational results for melt-processed Fe-hollandite, so related values were incidentally refined from the data reported by Utlak et al. [22] (Table S5 and 6) and are reported here.

Potential factors impacting thermodynamic stability

(a) Symmetry

Compositions of H1 and H2 which exhibited a *M–T* phase transition with increasing temperature were measured by DSC in order to quantitatively evaluate the effect of symmetry change on thermodynamic stability. As shown in Figure S5(a-b), no thermal peaks were observed for both H1 and H2 during their *M–T* phase transition, indicating that the enthalpic changes resulting from symmetry changes are small and indistinguishable from baseline heat flow or the quantity of enthalpic changes is below the detection limit of the DSC. This is not unexpected, as minor differences between materials having small symmetry differences are often negligible compared with the enthalpy of formation for many ceramic materials including $BaTiO_3$ perovskite and ZrO_2 [41, 42]. Therefore, symmetry in the present case has a minor impact on thermodynamic stability.

(b) Relative sizes of cations on A-sites and B-sites

Previous studies have stated that the enthalpic stability increased as R_B/R_A decreased [2, 23]. As shown in Fig. 6a, this trend is generally applicable for Fe-substituted hollandite in this work, although the enthalpy of formation of the Ba end member H1 is slightly more negative than predicted. Similar behavior was observed in Zn-substituted hollandite, which also exhibited a *M–T* phase transition with

increasing Cs content [5]. The mild enthalpic anomaly might arise from the phase transition and variation of local environments at the atomistic scale, such as different average Fe/Ti–O bond lengths, ordering/discording of A-site cations and vacancies in tunnels and different arrangements of B-site cations [2, 23, 43, 44].

(c) Tolerance factor

The thermodynamic stability of hollandite can be related to the tolerance factor [2, 23, 45] which for hollandite (t_H) can be calculated by using the following Eq. (2):

$$t_H = \frac{\left[(R_A + R_O)^2 - \frac{1}{2}(R_B + R_O)^2\right]^{\frac{1}{2}}}{\sqrt{\frac{3}{2}}(R_B + R_O)} \quad (2)$$

where R_A and R_B are the average ionic radii of A-site and B-site cations, respectively, and R_O is the oxygen ion radius [9, 45]. Using the R_A and R_B given in Table 2, t_H values of H1–H5 were calculated and are presented in Table 2. In Fig. 6b, the enthalpy of formation becomes more exothermic as t_H increases, indicating that enthalpic stability is improved with higher t_H within the t_H range of hollandite phase formation ($0.93 \le t_H \le 1.16$) [45].

(d) Optical basicity

According to previous studies, the thermodynamic stability may be affected by the optical basicity (Λ) [2, 46, 47]. The optical basicity of Fe-substituted hollandite (Λ_H) was calculated and given in Table 2 by using the expression and related Λ values from previous studies [2, 47]. Figure S6 displays that Λ_H values of H1–H5 are mostly unchanged across the compositional range. It is possible that the expected stronger basic character of the hollandite with higher Cs substitution is mitigated by the relatively strong optical basicity of Fe^{3+} on B-sites, which is slightly higher than that of Ti^{4+} [47]. Therefore, optical
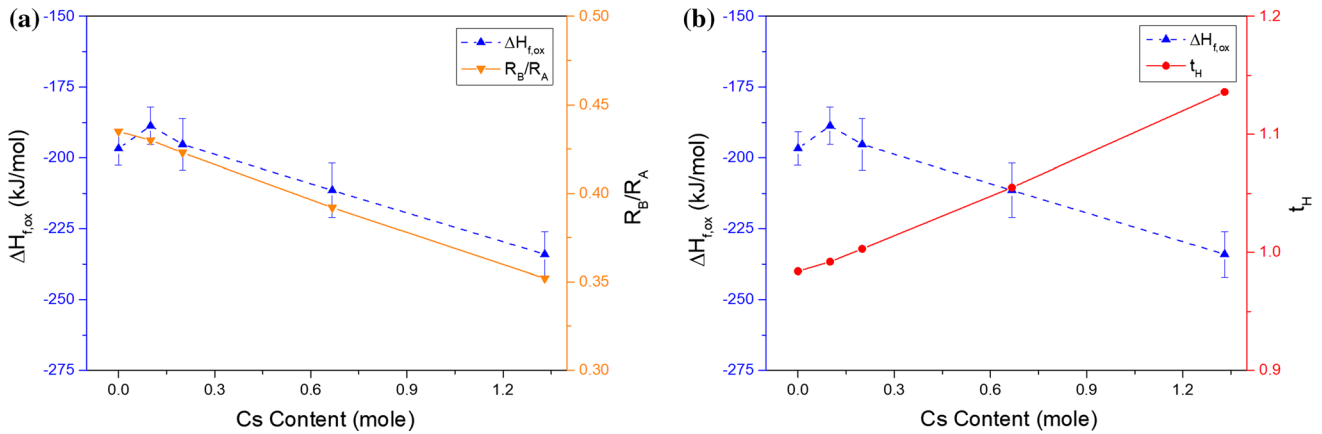
Figure 6 Variations of $\Delta H_{f,ox}$ and **a** R_B/R_A, **b** t_H for the five hollandites as a function of Cs substitutions.
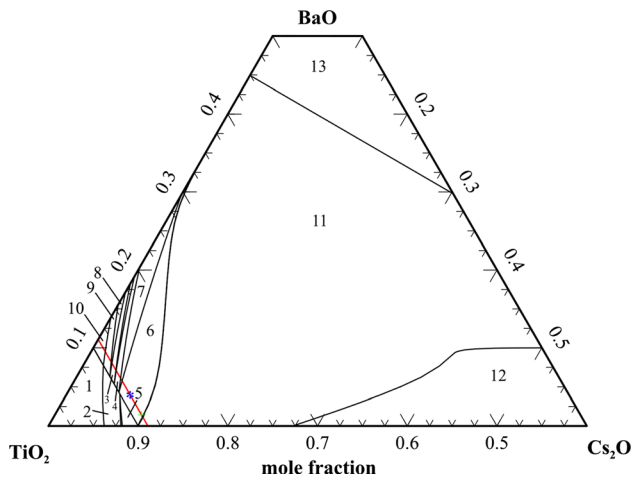

Figure 7 Computed 1200 °C isothermal phase diagram of pseudo-ternary BaO-Cs$_2$O-TiO$_2$ system with 10 mol% Fe$_2$O$_3$. Numbered phase regions are defined in Table 7.

Table 7 Stable phases in numbered regions of the 1200 °C isothermal BaO–Cs$_2$O–TiO$_2$ pseudo-ternary phase diagram with 10 mol% Fe$_2$O$_3$ in Fig. 7

Region	Stable phases
1	Fe$_2$TiO$_5$ + TiO$_2$ + Hollandite
2	Fe$_2$TiO$_5$ + Hollandite
3	Ba$_4$Ti$_{13}$O$_{30}$ + Hollandite
4	Ba$_6$Ti$_{17}$O$_{40}$ + Hollandite
5	Fe$_2$O$_3$ + Hollandite
6	BaTiO$_3$(β) + Hollandite
7	Ba$_6$Ti$_{17}$O$_{40}$ + BaTiO$_3$(β) + Hollandite
8	Ba$_2$Ti$_9$O$_{20}$ + Ba$_4$Ti$_{13}$O$_{30}$ + Hollandite
9	Ba$_2$Ti$_9$O$_{20}$ + Hollandite
10	Ba$_2$Ti$_9$O$_{20}$ + TiO$_2$ + Hollandite
11	BaTiO$_3$(β) + Liquid + Hollandite
12	Fe$_2$O$_3$ + Liquid + Hollandite
13	Ba$_2$TiO$_4$ + BaTiO$_3$(β) + Liquid + Hollandite

basicity does not affect thermodynamic stability of Fe-substituted hollandite.

Isothermal pseudo-ternary phase diagram

In Fig. 7, a computed BaO-Cs$_2$O-TiO$_2$ 1200 °C isothermal pseudo-ternary phase diagram with 10 mol% Fe$_2$O$_3$ was generated using the developed sublattice model and database (Fig. 7). Such models of the thermodynamic and phase equilibria can allow effective extrapolation to compositional regions that have not been yet experimentally determined [22, 48]. The diagram is computed here for 1200 °C for two reasons: (1) In this work, almost all hollandite samples were sintered at this temperature except the Ba end member H1 and (2) it has been confirmed that this temperature is high enough to synthesize single-

phase hollandite phase [4, 23, 24]. The diagram was truncated to display the composition region of interest and limit the extent or required model development which still adequately covering a reliable range over which to project hollandite phase stability.

The red composition line in Fig. 7 should share the hollandite formula Ba$_x$Cs$_y$Fe$_{1.6}$Ti$_{6.4}$O$_{16}$ with fixed 10 mol% Fe$_2$O$_3$ content and varying A-site occupancy. The previous study by Utlak et al. [22] concluded that there should be a high fraction of hollandite for the composition located at the boundary of two regions where both contain the hollandite phase, and naturally as well for regions with minimal secondary phases. The hollandite composition Ba$_{0.27}$Cs$_{1.06}$Fe$_{1.6}$Ti$_{6.4}$O$_{16}$ (H4|5) is indicated in Fig. 7 with a blue "*" within region No. 6 which also
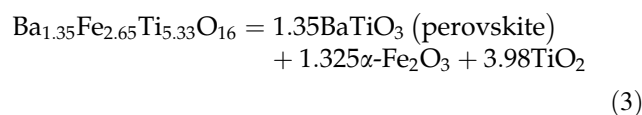
contains cubic $BaTiO_3$ (perovskite) as a secondary phase. Although computed to be stable at 1200 °C, the phase is not present at equilibrium at room temperature with high Cs_2O content hollandite, which will be demonstrated in "Implications for immobilization of tunnel cations" section. Therefore, H4|5 likely forms single-phase hollandites on cooling, which agrees well with both experimental and computational results. Furthermore, the optimal single-phase Fe-substituted hollandite-forming composition is predicted as $Cs_{1.42}Ba_{0.09}Fe_{1.6}Ti_{6.4}O_{16}$, symbolized as green "+", which has the theoretically highest Cs content and A-site occupancy.

Single-phase hollandite might also form in regions No. 3 and 9 intersected by the red composition line, because both of them only have one type of secondary phases. However, $Ba_2Ti_9O_{20}$ in compositions representative of region No. 9 was observed at room temperature in a previous study [9] and the hollandite in this region also has very low Cs loading, so it has limited utility as well. Although $Ba_4Ti_3O_{13}$ in the region No. 3 has not been reported in room temperature analyzed samples, it is very difficult to compare the phase stability between hollandite and $Ba_4Ti_3O_{13}$ due to the lack of a formation enthalpy from constituent oxides at room temperature for $Ba_4Ti_3O_{13}$. The composition in the region No. 3 as well has a much lower Cs content than that of region No. 6, thus not warranting further evaluation.

Implications for immobilization of tunnel cations

Strongly exothermic enthalpies of formation of H1–H5 indicate their excellent thermodynamic stability comparing to their binary constituent oxides, but one must also evaluate their stability with respect to other ternary oxides. Many possible ternary oxides in the hollandite-forming system have been described in Table 7 and Fig. 7. $BaTiO_3$ (perovskite) has to be considered as a potential competing phase as this phase is very likely to form at high temperature (in Fig. 7) and might be maintained along with hollandite upon cooling [2–5]. Cs–Fe–O, Cs–Ti–O, Ba–Fe–O, and Ba–Ti–O (excluding $BaTiO_3$ perovskite) systems are also possible phases, but they have not been reported at ambient conditions in non-melted processed samples using YSZ attrition balls. In addition, there are some controversies regarding the Fe–Ti–O system. Although some studies claimed that Fe_2TiO_5

was not stable at ambient conditions [2, 49], a recent study reported its appearance in the hollandite-forming system [9]. Nevertheless, the appearance of Fe_2TiO_5 does not result in a serious problem for the suitability of Fe-substituted hollandite because tunnel cations (i.e., Cs and Ba) are not incorporated in this phase. Therefore, it will not be considered in the subsequent analysis. Equations (3) and (4) were served as an example to illustrate how to evaluate phase stability and how to calculate the enthalpies of reaction (ΔH_{rxn}) at standard conditions of H1, respectively. This method has been used widely and is also applicable to H2–H4 [2–5].

$$Ba_{1.35}Fe_{2.65}Ti_{5.33}O_{16} = 1.35BaTiO_3 \, (\text{perovskite}) \\ + 1.325\alpha\text{-}Fe_2O_3 + 3.98TiO_2 \tag{3}$$

$$\Delta H_{rxn,H1} = 1.35\Delta H_{f,ox\,(BaTiO_3)} - \Delta H_{f,ox(H1)} \\ = -8.93 \pm 8.89 \, \text{kJ/mol} \tag{4}$$

where the $\Delta H_{f,ox(H1)}$ value was given in Table 3 and $\Delta H_{f,ox(BaTiO3)} = -152.3 \pm 4.0$ kJ/mol [41]. Thus, ΔH_{rxn} values of H1–H4 were calculated and listed in Table 3 as well.

In Fig. 8, it can be concluded that H3 and H4 are energetically stable at room temperature with respect to $BaTiO_3$ (perovskite), Cs_2O, $\alpha\text{-}Fe_2O_3$, and TiO_2, because their ΔH_{rxn} values are endothermic. In contrast, H1 is not stable with respect to $BaTiO_3$ (perovskite), $\alpha\text{-}Fe_2O_3$, and TiO_2, since the ΔH_{rxn} value is exothermic. In addition, because the entropy change in a reaction involving solid phases is small, the
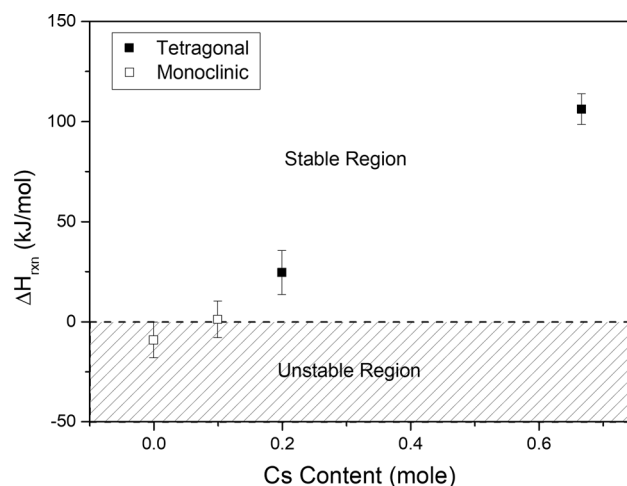

Figure 8 Variations of ΔH_{rxn} for H1–H4 as a function of Cs substitutions.
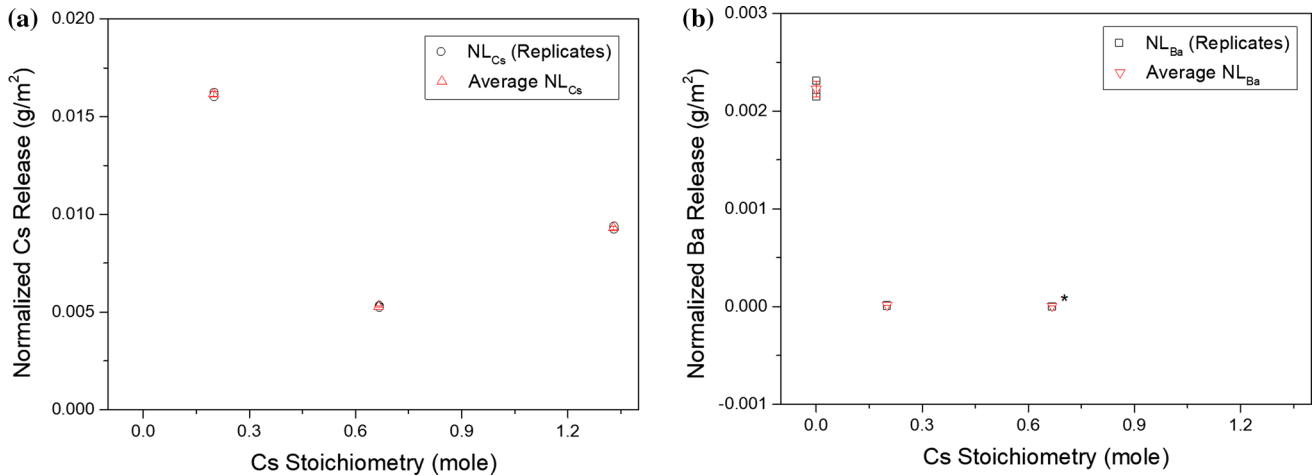
Figure 9 NL and average NL of **a** Cs and **b** Ba for Fe-substituted hollandite samples with different Cs contents. Error bars of average NL stand for standard deviations (*Note* NL_{Ba} and average NL_{Ba} denoted as "*" in (**b**) roughly showed their order of magnitude because their actual values were even smaller and lower than the detection limit of ICP-AES).

Gibbs free energy is expected to be positive and hence not favorable [2]. Furthermore, the phase stability of H2 may be comparable to $BaTiO_3$ (perovskite), Cs_2O, α-Fe_2O_3, and TiO_2, because its ΔH_{rxn} value is very close to zero within experimental uncertainties [2]. These estimates provide convincing evidence that higher Cs substitution stabilize the hollandite phase.

Chemical durability

Leaching resistance of Cs and Ba in Fe-substituted hollandite was evaluated by leaching tests. Detailed experimental data of sample matrix was summarized in Table S7. Normalized Cs and Ba release values for each composition are given in Table S7. In Fig. 9a, the normalized Cs release (NL_{Cs}) values are significantly improved for the high Cs content H4 and Cs end member H5 compared with that of the low Cs content H2. A similar trend is observed in Fig. 9b where results of the normalized Ba release (NL_{Ba}) show that almost all Ba cations were retained in H3 and H4 while the H1 resulted in much higher Ba release. Consequently, it is apparent that increasing the Cs content results in improved leaching resistance of tunnel cations (i.e., Cs and Ba) in Fe-substituted hollandite.

It is noteworthy that the most energetically stable composition H5 does not exhibit the least NL_{Cs}. A similar phenomenon has been reported in Ga-substituted hollandite [4]. The nonlinear correlation between thermodynamic stability and chemical durability may be due to a "threshold" effect of Cs substitution. This correlation will be examined in future work by the investigation of additional B-site compositions and the aid of phase diagrams generated from the sublattice computational model.

Conclusion

A series of Fe-substituted hollandite compositions were studied across the A-site solid solution from Ba end member to Cs end member. A phase transition from monoclinic to tetragonal symmetry could be induced by both Cs substitution and heating. Cs volatilization during processing was also reduced in compositions with higher targeted Cs content. Fe-substituted hollandite with higher Cs contents were more thermodynamically stable with respect to their binary constituent oxides as well as to other competing phase assemblages, which agreed well with sublattice model predictions. Moreover, a decreasing R_B/R_A and increasing tolerance factor with Cs substitution contributed to the enhanced thermodynamic stability. According to a reoptimized sublattice model, a pseudo-ternary diagram was computed extrapolating the phase equilibrium behavior of the hollandite-forming system to regions that had not been experimentally addressed. Results of leaching test confirmed that high Cs content stabilized

hollandite phase, although the more explicit correlation between thermodynamic stability and chemical durability is still needed to be addressed in future work.

Acknowledgements

Electronic supplementary material: The online version of this article (https://doi.org/10.1007/s10853-020-04447-3) contains supplementary material, which is available to authorized users.

References

[1] Ringwood AE, Kesson SE, Ware NG, Hibberson W, Major A (1979) Immobilisation of high level nuclear reactor wastes in SYNROC. Nature 278:219–223

[2] Costa GC, Xu H, Navrotsky A (2013) Thermochemistry of barium hollandites. J Am Ceram Soc 96(5):1554–1561

[3] Xu H, Wu L, Zhu J, Navrotsky A (2015) Synthesis, characterization and thermochemistry of Cs-, Rb-and Sr-substituted barium aluminium titanate hollandites. J Nucl Mater 459:70–76

[4] Zhao M, Xu Y, Shuller-Nickles L, Amoroso J, Frenkel AI, Li Y, Gong W, Lilova K, Navrotsky A, Brinkman KS (2019) Compositional control of radionuclide retention in hollandite-based ceramic waste forms for Cs-immobilization. J Am Ceram Soc 102(7):4314–4324

[5] Grote R, Zhao M, Shuller-Nickles L, Amoroso J, Gong W, Lilova K, Navrotsky A, Tang M, Brinkman KS (2019) Compositional control of tunnel features in hollandite-based ceramics: structure and stability of $(Ba,Cs)_{1.33}(Zn,Ti)_8O_{16}$. J Mater Sci 54(2):1112–1125. https://doi.org/10.1007/s10853-018-2904-1

[6] Levins DM, Smart RSC (1984) Effects of acidification and complexation from radiolytic reactions on leach rates of SYNROC C and nuclear waste glass. Nature 309:776–778

[7] Cheary RW (1988) The immobilisation of cesium in synroc. Mater Sci Forum 27(28):397–406

[8] Cheary RW (1986) An analysis of the structural characteristics of hollandite compounds. Acta Crystallogr B 42:229–236

[9] Aubin-Chevaldonnet V, Caurant D, Dannoux A, Gourier D, Charpentier T, Mazerolles L, Advocat T (2007) Preparation and characterization of $(Ba, Cs)(M, Ti)_8O_{16}$ ($M = Al^{3+}$, Fe^{3+}, Ga^{3+}, Cr^{3+}, Sc^{3+}, Mg^{2+}) hollandite ceramics developed for radioactive cesium immobilization. J Nucl Mater 366(1–2):137–160

[10] Tumurugoti P, Sundaram S, Misture ST (2018) Cesium immobilization in (Ba,Cr)-hollandites: effects on structure. J Solid State Chem 258:72–78

[11] Bailey DJ, Stennett MC, Mason AR, Hyatt NC (2018) Synthesis and characterisation of the hollandite solid solution $Ba_{1.2−x}Cs_xFe_{2.4−x}Ti_{5.6+x}O_{16}$ for partitioning and conditioning of radiocaesium. J Nucl Mater 503:164–170

[12] Xu H, Costa GC, Stanek CR, Navrotsky A (2015) Structural behavior of $Ba_{1.24}Al_{2.48}Ti_{5.52}O_{16}$ hollandite at high temperature: an in situ neutron diffraction study. J Am Ceram Soc 98(1):255–262

[13] Tumurugoti P, Sundaram S, Brinkman KS, Amoroso J, Fox K (2014) Melt-processed multiphasic ceramic waste forms. Adv Mater Sci Environ Energy Technol III 250:205–212

[14] Amoroso J, Marra J, Conradson SD, Tang M, Brinkman K (2014) Melt processed single phase hollandite waste forms for nuclear waste immobilization: $Ba_{1.0}Cs_{0.3}A_{2.3}Ti_{5.7}O_{16}$; A = Cr, Fe, Al. J Alloys Compd 584:590–599

[15] Shannon RD (1976) Revised effective ionic radii and systematic studies of interatomic distances in halides and chalcogenides. Acta Crystallogr A 32(5):751–767

[16] Carter M, Vance E, Li H (2003) Hollandite-rich ceramic melts for the immobilisation of Cs. MRS Online Proc Libr Arch 807:249. https://doi.org/10.1557/PROC-807-249

[17] Carter M, Vance E, Mitchell D, Hanna J, Zhang Z, Loi E (2002) Fabrication, characterization, and leach testing of hollandite, $(Ba, Cs)(Al, Ti)_2Ti_6O_{16}$. J Mater Res 17(10):2578–2589

[18] Navrotsky A (1997) Progress and new directions in high temperature calorimetry revisited. Phys Chem Miner 24(3):222–241

[19] Navrotsky A (2014) Progress and new directions in calorimetry: a 2014 perspective. J Am Ceram Soc 97(11):3349–3359

[20] ASTM International (2014) C1285-14 standard test methods for determining chemical durability of nuclear, hazardous,

and mixed waste glasses and multiphase glass ceramics: the product consistency test (PCT). West Conshohocken, PA

[21] Amoroso J, Marra JC, Tang M, Lin Y, Chen F, Su D, Brinkman KS (2014) Melt processed multiphase ceramic waste forms for nuclear waste immobilization. J Nucl Mater 454(1–3):12–21

[22] Utlak SA, Besmann TM, Brinkman KS, Amoroso JW (2019) Thermodynamic assessment of the hollandite high-level radioactive waste form. J Am Ceram Soc 102(10):6284–6297

[23] Xu Y, Feygenson M, Page K, Nickles LS, Brinkman KS (2016) Structural evolution in hollandite solid solutions across the A-site compositional range from $Ba_{1.33}Ga_{2.66-}Ti_{5.34}O_{16}$ to $Cs_{1.33}Ga_{1.33}Ti_{6.67}O_{16}$. J Am Ceram Soc 99(12):4100–4106

[24] Xu Y, Wen Y, Grote R, Amoroso J, Nickles LS, Brinkman KS (2016) A-site compositional effects in Ga-doped hollandite materials of the form $Ba_xCs_yGa_{2x+y}Ti_{8-2x-y}O_{16}$: implications for Cs immobilization in crystalline ceramic waste forms. Sci Rep 6:27412. https://doi.org/10.1038/srep27412

[25] Grote R, Hong T, Shuller-Nickles L, Amoroso J, Tang M, Brinkman KS (2019) Radiation tolerant ceramics for nuclear waste immobilization: structure and stability of cesium containing hollandite of the form $(Ba,Cs)_{1.33}(Zn,Ti)_8O_{16}$ and $(Ba,Cs)_{1.33}(Ga,Ti)_8O_{16}$. J Nucl Mater 518:166–176

[26] Post JE, Von Dreele RB, Buseck PR (1982) Symmetry and cation displacements in hollandites: structure refinements of hollandite, cryptomelane and priderite. Acta Crystallogr B 38:1056–1065

[27] Zhang J, Burnham CW (1994) Hollandite-type phases: geometric consideration of unit-cell size and symmetry. Am Miner 79(1–2):168–174

[28] Ishii M, Fujiki Y, Ohsaka T (1985) Raman scattering in one-dimensional ionic conductors Rb-priderites. Solid State Commun 55(12):1123–1126

[29] Ohsaka T, Fujiki Y (1982) Raman spectra in hollandite type compounds $K_{1.6}Mg_{0.8}Ti_{7.2}O_{16}$ and $K_{1.6}Al_{1.6}Ti_{6.4}O_{16}$. Solid State Commun 44(8):1325–1327

[30] Roy N, Park Y, Sohn Y, Leung KT, Pradhan D (2014) Green synthesis of anatase TiO_2 nanocrystals with diverse shapes and their exposed facets-dependent photoredox activity. ACS Appl Mater Interfaces 6(19):16498–16507

[31] Porto S, Fleury P, Damen T (1967) Raman spectra of TiO_2, MgF_2, ZnF_2, FeF_2, and MnF_2. Phys Rev 154(2):522–526

[32] Shibata Y, Suemoto T, Ishigame M (1986) Raman scattering studies of mobile ions in superionic conductor hollandites. Phys Status Solidi (B) 134(1):71–79

[33] Poyraz AS, Huang J, Pelliccione CJ, Tong X, Cheng S, Wu L, Zhu Y, Marschilok AC, Takeuchi KJ, Takeuchi ES (2017) Synthesis of cryptomelane type α-MnO_2 ($K_xMn_8O_{16}$) cathode materials with tunable K^+ content: the role of tunnel cation concentration on electrochemistry. J Mater Chem A 5(32):16914–16928

[34] Knyazev AV, Mączka M, Ladenkov IV, Bulanov EN, Ptak M (2012) Crystal structure, spectroscopy, and thermal expansion of compounds in M_2^IO–Al_2O_3–TiO_2 system. J Solid State Chem 196:110–118

[35] Ushakov SV, Cheng J, Navrotsky A, Wu JR, Haile SM (2002) Formation enthalpies of tetravalent lanthanide perovskites by high temperature oxide melt solution calorimetry. MRS Online Proc Libr Arch 718(D7):17. https://doi.org/10.1557/PROC-718-D7.17

[36] Ushakov SV, Navrotsky A, Farmer JM, Boatner LA (2004) Thermochemistry of the alkali rare-earth double phosphates, $A_3RE(PO_4)_2$. J Mater Res 19(7):2165–2175

[37] Majzlan J, Navrotsky A, Neil JM (2002) Energetics of anhydrite, barite, celestine, and anglesite: a high-temperature and differential scanning calorimetry study. Geochim Cosmochim Acta 66(10):1839–1850

[38] Putnam RL, Navrotsky A, Woodfield BF, Boerio-Goates J, Shapiro JL (1999) Thermodynamics of formation for zirconolite ($CaZrTi_2O_7$) from T = 298.15 K to T = 1500 K. J Chem Therm 31(2):229–243

[39] Robie RA, Hemingway BS (1995) Thermodynamic properties of minerals and related substances at 298.15 K and 1 Bar (10^5 Pascals) pressure and at higher temperatures. U.S. Geological Survey Bulletin 2131; U.S. G.P.O., Washington

[40] Wu L, Schliesser J, Woodfield BF, Xu H, Navrotsky A (2016) Heat capacities, standard entropies and Gibbs energies of Sr-, Rb-and Cs-substituted barium aluminotitanate hollandites. J Chem Thermodyn 93:1–7

[41] Takayama-Muromachi E, Navrotsky A (1988) Energetics of compounds ($A^{2+}B^{4+}O_3$) with the perovskite structure. J Solid State Chem 72(2):244–256

[42] Chase MWJ (1998) NIST-JANAF thermochemical tables. American Institute of Physics, University Park, MD. https://janaf.nist.gov/. Accessed 6 Nov 2019

[43] Rane MV, Navrotsky A, Rossetti GA Jr (2001) Enthalpies of formation of lead zirconate titanate (PZT) solid solutions. J Solid State Chem 161(2):402–409

[44] Wen Y, Xu Y, Brinkman KS, Shuller-Nickles L (2018) Atomistic scale investigation of cation ordering and phase stability in Cs-substituted $Ba_{1.33}Zn_{1.33}Ti_{6.67}O_{16}$, $Ba_{1.33}Ga_{2.66}Ti_{5.67}O_{16}$ and $Ba_{1.33}Al_{2.66}Ti_{5.33}O_{16}$ hollandite. Sci Rep 8:5003. https://doi.org/10.1038/s41598-018-22982-7

[45] Kesson S, White T (1986) Radius ratio tolerance factors and the stability of hollandites. J Solid State Chem 63(1):122–125

[46] Duffy JA (2006) Ionic–covalent character of metal and nonmetal oxides. J Phys Chem A 110(49):13245–13248

[47] Lebouteiller A, Courtine P (1998) Improvement of a bulk optical basicity table for oxidic systems. J Solid State Chem 137(1):94–103

[48] Lukas H, Fries SG, Sundman B (2007) Computational thermodynamics: the Calphad method. Cambridge University Press, New York

[49] Navrotsky A (1975) Thermodynamics of formation of some compounds with the pseudobrookite structure and of the $FeTi_2O_5$–Ti_3O_5 solid solution series. Am Miner 60(3–4):249–256